frontiers | Frontiers in Physics

TYPE Original Research
PUBLISHED 15 August 2022
DOI 10.3389/fphy.2022.971360

High-dimensional orbital angular momentum entanglement from an ultrathin nonlinear film

Fan Dai[1], Shuang-Yin Huang[1], Min Wang[1], Chenghou Tu[1], Yongnan Li[1]* and Hui-Tian Wang[2,3]*

[1]Key Laboratory of Weak-Light Nonlinear Photonics and School of Physics, Nankai University, Tianjin, China, [2]National Laboratory of Solid State Microstructures, Nanjing University, Nanjing, China, [3]Collaborative Innovation Center of Advanced Microstructures, Nanjing University, Nanjing, China

Check for updates

OPEN ACCESS

EDITED BY
Carlo Ottaviani,
University of York, United Kingdom

REVIEWED BY
Gustavo Cañas,
University of the Bío Bío, Chile
Yijie Shen,
University of Southampton,
United Kingdom

*CORRESPONDENCE
Yongnan Li,
liyongnan@nankai.edu.cn
Hui-Tian Wang,
htwang@nju.edu.cn

SPECIALTY SECTION
This article was submitted to Quantum Engineering and Technology, a section of the journal Frontiers in Physics

RECEIVED 17 June 2022
ACCEPTED 15 July 2022
PUBLISHED 15 August 2022

CITATION
Dai F, Huang S-Y, Wang M, Tu C, Li Y and Wang H-T (2022), High-dimensional orbital angular momentum entanglement from an ultrathin nonlinear film.
Front. Phys. 10:971360.
doi: 10.3389/fphy.2022.971360

Entanglement, as a crucial feature of quantum systems, is essential for various applications of quantum technologies. High-dimensional entanglement has the potential to encode arbitrary large amount of information and enhance robustness against eavesdropping and quantum cloning. The orbital angular momentum (OAM) entanglement can achieve the high-dimensional entanglement nearly for free stems due to its discrete and theoretically infinite-dimensional Hilbert space. A stringent limitation, however, is that the phase-matching condition limits the entanglement dimension because the coincidence rate decreases significantly for high-order modes. Here we demonstrate relatively flat high-dimensional OAM entanglement based on a spontaneous parametric down conversion (SPDC) from an ultrathin nonlinear lithium niobite crystal. The difference of coincidences between the different-order OAM modes significantly decreases. To further enhance the nonlinear process, this microscale SPDC source will provide a promising and integrated method to generate optimal high-dimensional OAM entanglement.

KEYWORDS

orbital angular momentum, quantum entanglement, high-dimensional entanglement, nonlinear film, phase matching

1 Introduction

Light with a helical phase exp $(im\phi)$, which carries orbital angular momentum (OAM), has attracted close attention in the last few decades and found numerous photonic applications, such as high density data storage [1, 2], optical imaging [3–8], holography [9, 10], astrophysics [11, 12], optical manipulation [13–15] and in the optical interferometer for the detection of gravitational waves [16]. In addition, the OAM of light serves, in a sense, as an "alphabet" that allows information to be encoded into the spatial wavefunction of light. The key motivation is that the OAM has potentially an unlimited number of states [17, 18]. In the classical domain, the OAM can increase the capacity of optical communication links ranging from implementation in fibre [19, 20], over-city links [21] and free-space [22], and can also operate in mm-wave [23]. Actually, each OAM mode can be considered as an individual quantum degree of freedom [24, 25]. Quantum mechanically, the OAM occurs in discrete values of $m\hbar$ per photon, where m is in

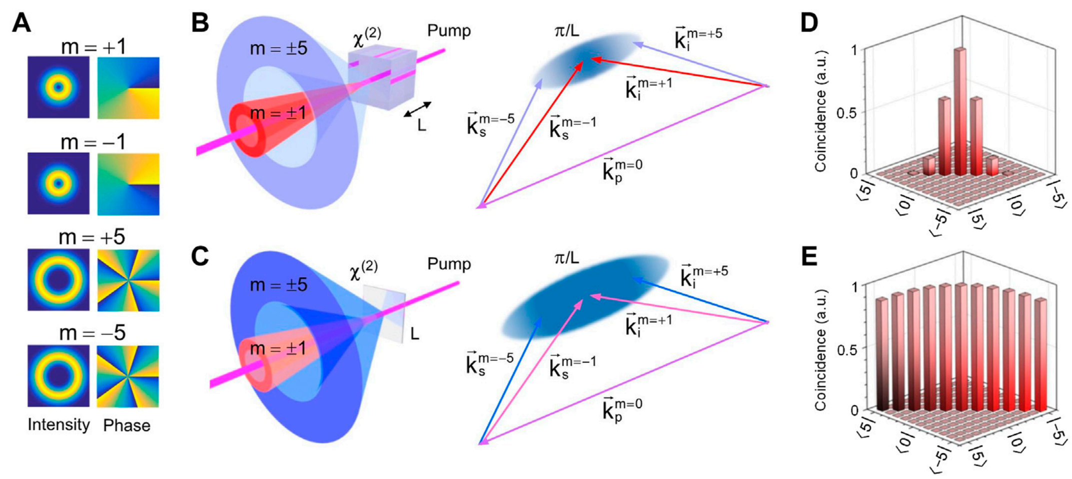

FIGURE 1
(A) The intensity and phase for OAM $|m| = 1$ and $|m| = 5$. High-dimensional OAM entanglement from the type-0 SPDC in a thick **(B)** and ultrathin **(C)** nonlinear LN crystal orthogonal to the pump **(D)** and **(E)** is the simulated spiral spectrum of 11-dimensional OAM entanglement in the nonlinear LN crystal with length of $L = 0.6$ *mm* and $L = 6$ *μm* respectively. The pump is a Gaussian mode $m = 0$. The coincidences of the different OAM state are normalized by the coincidence at OAM $m = 0$.

principle an unbounded integer. The OAM opens many promising perspectives for quantum communication and computation [26, 27]. Zeilinger's group firstly realized the OAM-entangled photon pair [28] and verified that the maximum dimension of the OAM entanglement can reach 10,000 [29], which shows the great potential and novel advantage in the high-dimensional quantum information such as teleportation [30] and quantum communication [31–33]. A spontaneous parametric down conversion (SPDC) process is the most common workhorse for the generation of the OAM-entangled photon pairs [34, 35]. Albeit convenient, this process exhibits several drawbacks. For example, photon pairs generated in this way have a non-uniform OAM distribution, which constrains the increase of dimension [26]. The entanglement property of the OAM states is determined by the overlap between the transverse modes of the pump and photon pairs because the transverse intensity profile of the OAM mode depends on its topological charge m. The dimensionality of the two-photon OAM states can be increased with the use of perfect optical vortex (POV) in the pump because the POV is a class of size-invariant modes [36, 37]. The versatile high-dimensional quantum states are generated by using the structured pump [38–40]. Recently, the entangled OAM photon pairs are generated in the multiple SPDC processes by the path identity [41].

In addition, the non-uniformity of OAM entanglement is also restricted by the longitudinal phase mismatching. High-order OAM modes have the larg phase mismatch, which leads to the low generation efficiency. This restriction can be improved by utilizing the microscale flat-optics quantum source [42]. Here we have achieved relatively flat high-dimensional OAM entanglement in an ultrathin film of lithium niobite (LN) via the SPDC, which is impossible in a single bulk source. Being free from the phase matching constraints, the ultrathin source can be fabricated of any materials with large second-order susceptibility. Our method provides a new platform of high-dimensional OAM entanglement on which to investigate fundamental quantum effects but it also has practical applications.

2 Theory

In the paraxial approximation, photons carrying OAM can be described by a Laguerre-Gaussian mode LG_p^m. The radial index p shows the number of radial zero crossings and the azimuthal index m is the topological winding number, corresponding to OAM carried by the mode, $m\hbar$ per photon. Figure 1A shows the intensity and phase distributions of the LG modes with different OAM. A typical SPDC process, which a Gaussian beam propagating along the x direction pumps a nonlinear crystal with a length of L, as shown in Figure 1B, produces a pair of highly correlated, lower-frequency photons, commonly termed signal and idler photons. The generated two-photon quantum state by the SPDC is given by [43].

$$|\psi\rangle = \iint d\mathbf{k}_s d\mathbf{k}_i \Phi(\mathbf{k}_s, \mathbf{k}_i)\hat{a}_s^\dagger(\mathbf{k}_s)\hat{a}_i^\dagger(\mathbf{k}_i)|0\rangle, \tag{1}$$

where $|0\rangle$ is the multimode vacuum state, while $\hat{a}_s^\dagger(\mathbf{k}_s)$ and $\hat{a}_i^\dagger(\mathbf{k}_i)$ are creation operators for the signal and idler modes with the transversal wave vectors $\mathbf{k}_s$ and $\mathbf{k}_i$, respectively. $\Phi(\mathbf{k}_s, \mathbf{k}_i)$ represents the joint amplitude with the following structure

$$\Phi(\mathbf{k}_s, \mathbf{k}_i) \propto F(\mathbf{k}_s, \mathbf{k}_i)\mathrm{sinc}(\Delta kL/2), \tag{2}$$

where $F(\mathbf{k}_s, \mathbf{k}_i)$ describes the mode function of the Gaussian pump beam at the input face of the nonlinear crystal. Here we consider only LG modes with $p = 0$, correspondingly we simplify as $\mathrm{LG}_p^m \rightarrow \mathrm{LG}_m$. One can decompose the quantum state $|\psi\rangle$ in the base of the eigenstates of the OAM operator under the OAM conservation as

$$|\psi\rangle = \sum_m C_{m,-m}|m\rangle_s|-m\rangle_i \tag{3}$$

where $|m\rangle_s$ and $|-m\rangle_i$ correspond to the signal and idler modes, respectively. The coincidence amplitudes $C_{m,-m}$ is written as

$$C_{m,-m} = \iint d\mathbf{k}_s d\mathbf{k}_i \Phi(\mathbf{k}_s, \mathbf{k}_i)\mathrm{LG}_m(\mathbf{k}_s)\mathrm{LG}_{-m}(\mathbf{k}_i), \tag{4}$$

where $\mathrm{LG}_m(\mathbf{k})$ is the Laguerre-Gaussian mode function in the spatial frequency domain at $x = 0$. The coincidence probability is $P_{m,-m} = |C_{m,-m}|^2$, which gives the value of the joint detection probability for finding one photon in the signal mode $|m\rangle_s$ and one photon in the idler mode $|-m\rangle_i$. It is clear that the coincidence probability $P_{m,-m}$ is mainly determined by the phase matching. If the $|0\rangle_s|0\rangle_i$ mode is assumed to be phase matched, the phase mismatching of high-order OAM modes can be calculated analytically as [42].

$$\Delta kL\Big/2 \propto -|m|\frac{\pi L}{4\lambda}\frac{\omega_0^2}{z_R^2}\left(1 - \frac{2z_R}{L}\arctan\frac{L}{2z_R}\right), \tag{5}$$

where z_R is the Rayleigh range of the mode $|0\rangle_s|0\rangle_i$ and ω_0 is the beam waist of the down-converted beam, respectively. For a type-0 degenerate phase matching process, $\lambda_s = \lambda_i = 2\lambda_p$ is satisfied. We use a common value of $\lambda = 2\lambda_p$ to replace λ_s and λ_i. According to Eq. 5, the phase mismatching increase with the topological charge m of the down-converted photon because the high-order modes have a larger divergence angle, which will decrease the longitudinal component of the wave vector, as shown in Figure 1B. Comparing with the mode $|1\rangle_s|-1\rangle_i$, the mode $|5\rangle_s|-5\rangle_i$ suffers from the larger longitudinal phase mismatching and has the lower coincidence probability. In this case, the longer nonlinear crystal will further increase the difference of the coincidence probabilities between the different OAM modes, although it can improve the total efficiency of the photon pairs generated by the SPDC. We calculate the spiral spectrum of the high-dimensional OAM entanglement for the LN crystal with L = 0.6 mm, as shown in Figure 1D. The brightness of photons greatly decreases for the high-order OAM modes, which often limits the usefulness of the high-dimensional OAM entangled states in the quantum experiment. When the length of the nonlinear crystal decreases to $L = 6$ μm, as shown in Figure 1C, the difference of coincidence probabilities between the different OAM modes is dramatically reduced and the spiral spectrum becomes flat, as shown in Figure 1E. The ultrathin nonlinear crystal not only allows very large longitudinal mismatch, but also leads to a very broad spectrum of emitted photons, both in frequency and in angle [42].

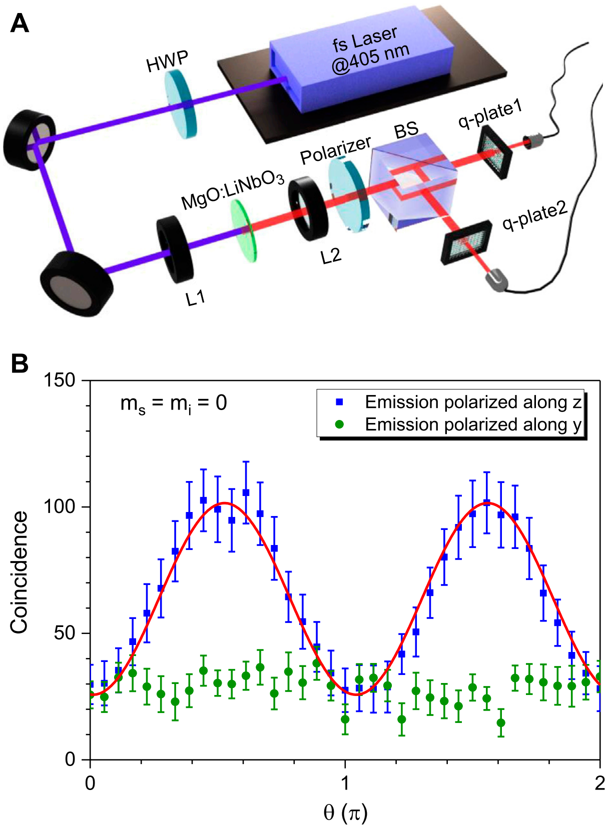

FIGURE 2
(A) The setup used to detect SPDC from the x-cut ultrathin LN film. The pump power is 250 mw. HWP: halfwave plate, BS: beam splitter, L1 and L2: lens **(B)** The coincidence rate of the fundamental mode (m = 0) versus the pump polarization direction, for the emission polarized along z (blue squares, red fit) and along y (green triangles). θ is the angle between the pump polarization and the y axis. The coincidence time is 1s.

3 Experimental results

As the experimental setup shown in Figure 2A, we use an x-cut ultrathin film of MgO-doped LN on a fused silica substrate as a nonlinear medium. The LN ultrathin slice had a thickness of ~6 μm. The pump source is a femtosecond (fs) pulsed laser at a central wavelength of 405 nm, with a pulse duration of ~140 fs and a repetition rate of ~80 MHz to create photon pairs at a degenerate wavelength of 810 nm by the SPDC. Benefiting from the largest element d_{33} of the nonlinear susceptibility tensor, the polarization of the pump fs laser is oriented along the z axis of the

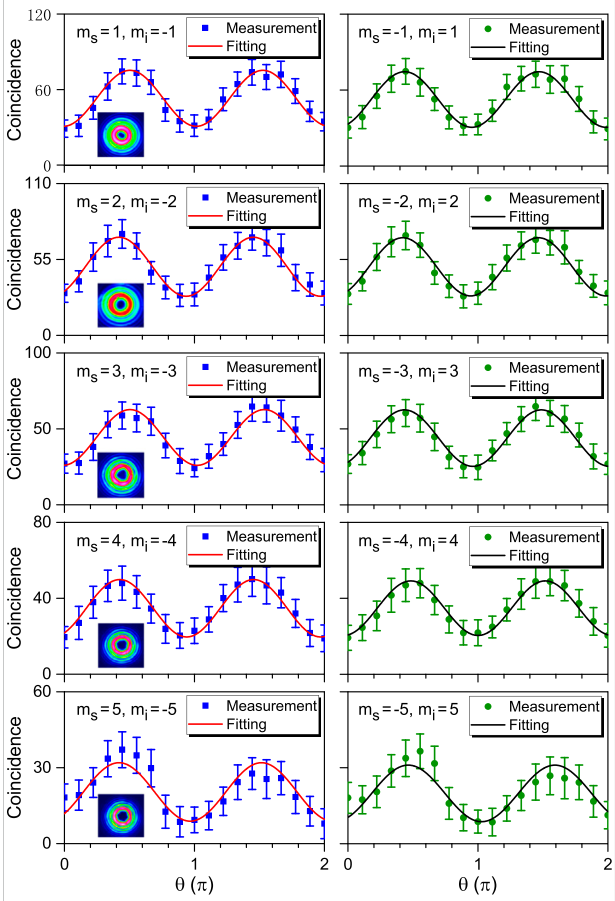

FIGURE 3
The coincidence rate versus the pump polarization direction for different mode combinations of the signal and idler photons from the SPDC. θ is the angle between the pump polarization and the *y* axis. The coincidence time is 1*s*. The insets are the intensity distributions for corresponded OAM.

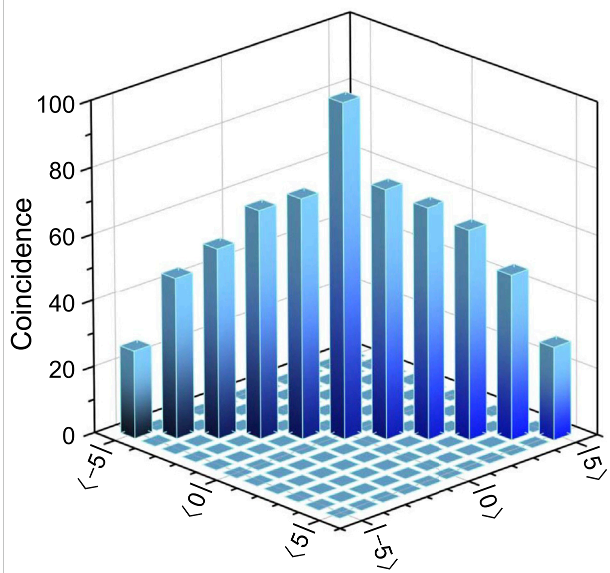

FIGURE 4
The measured spiral spectrum of 11-dimensional OAM entanglement from the SPDC in the ultrathin LN film. The coincidence time is 1*s*.

ultrathin LN film. Under the condition of type-0 degenerate collinear phase matching, down-conversion photon pairs have the same polarization. The 10 nm narrow bandwidth interference filters (centred at the wavelength of 810 nm) are used to improve the spectral purity of the correlated photon pairs and to block the remaining pump.

To confirm that the SPDC was mediated by the d_{33} element of the nonlinear susceptibility tensor, with the pump, signal, and idler photons all polarized along the *z* axis, we have measured the polarization dependence of the coincidence count, as shown in Figure 2B. The coincidence count depends on the angle θ between the pump polarization and the *y* axis as $\sin^2\theta$ (blue squares, red fitting curve) and reaches the maximum value only when the signal and idler photons are polarized along the *z* axis. In contrast, for the emission polarized along the *y* axis, almost no real coincidences were observed (green circles). Then we use two separate *q*-plates to transform the incoming field to a fundamental Gaussian mode, which is the unique mode that can be coupled into the single mode fibers, for measuring the OAM of the photon pairs. In the collinear configuration, OAM is conserved in the SPDC, hence we expect the OAMs of the signal and idler photons to be anticorrelated, i.e., the coincidence count is high only when $m_s = -m_i$. Figure 3 shows the measured coincidence counts for different combinations of signal and idler photon modes. For each combination the polarization-dependent coincidence counts verifies that the correlated photon pairs are generated from the ultrathin LN by the SPDC. Figure 4 shows the spiral spectrum of the 11-dimensional OAM entanglement and it becomes relatively flat comparing with thick nonlinear crystal. The measured coincidence of the high-order OAM state is lower comparing with the theoretical simulation because the collection efficiency decreases with the increment of the OAM sate. In addition, we observe that the SPDC of ultrathin crystal has better robustness for the position of the pump. When the crystal shift 1 *mm* from the focus of the pump, the decrease of the maximum coincidence counts for difference mode of photon pairs is about 5%.

4 Conclusion

In conclusion, we have demonstrated the relatively flat high-dimensional OAM entanglement based on the SPDC in the ultrathin LN crystal which allows large longitudinal phase mismatching and decreases the difference of coincidence rate between the different OAM mode. This state might be required for quantum experiment. Although we use the highest nonlinear component available in LN, but the efficiency remained much lower than for phase-matched SPDC in a macroscopic crystal. The generation efficiency can be optimised by using the nonlinear material with the giant second-harmonic generation [45]. Recently, metasurfaces offer an ultracompact and versatile platform for enhancing nonlinear optical processes by designing Bound State in the Continuum (BIC) resonances, which support a high confinement of the optical field within the nonlinear material [46, 47]. Then SPDC efficiency can be dramatically increased when the signal and idler photons are supported by BIC resonances [48] to generate high-dimensional hyperentanglement in the frequency and OAM regimes for increasing the quantum information capacity.

Data availability statement

The original contributions presented in the study are included in the article/Supplementary Material, further inquiries can be directed to the corresponding authors.

Author contributions

FD, YL, and H-TW designed experiments, FD performed the theoretical simulations FD dominantly and MW assistantly carried out experiments and analyzed data. FD, YL, and H-TW wrote the manuscript. YL and H-TW. planned and supervised the project. All authors discussed the results.

Funding

This work was supported financially by the National Key R&D Program of China (2019YFA0705000, 2019YFA0308700, 2020YFA0309500), the National Natural Science Foundation of China (12074197, 12074196, 11922406). The authors would like to thank the support by Collaborative Innovation Center of Extreme Optics.

Conflict of interest

The authors declare that the research was conducted in the absence of any commercial or financial relationships that could be construed as a potential conflict of interest.

Publisher's note

References

1. Ren H-R, Li X-P, Zhang Q-M, Gu M. On-chip noninterference angular momentum multiplexing of broadband light. *Science* (2016) 352:805–9. doi:10.1126/science.aaf1112

2. Xu O-Y, Xu Y, Xian M-C, Feng Z-W, Zhu L-W, Cao Y-Y, et al. Synthetic helical dichroism for six-dimensional optical orbital angular momentum multiplexing. *Nat Photon* (2021) 15:901–7. doi:10.1038/s41566-021-00880-1

3. Hell SW, Wichmann J. Breaking the diffraction resolution limit by stimulated emission: Stimulated-emission-depletion fluorescence microscopy. *Opt Lett* (1994) 19:780. doi:10.1364/OL.19.000780

4. Torner L, Torres JP, Carrasco S. Digital spiral imaging. *Opt Express* (2005) 13:873. doi:10.1364/OPEX.13.000873

5. Liu K, Cheng Y-Q, Gao Y, Li X, Qin Y-L, Wang H-Q, et al. Super-resolution radar imaging based on experimental oam beams. *Appl Phys Lett* (2017) 110:164102. doi:10.1063/1.4981253

6. Chu J-Q, Li X-F, Smithwick Q, Chu D-P. Coding/decoding two-dimensional images with orbital angular momentum of light. *Opt Lett* (2016) 41:1490. doi:10.1364/OL.41.001490

7. Lee MP, Gibson GM, Bowman R, Bernet S, Ritsch-Marte M, Phillips DB, et al. A multi-modal stereo microscope based on a spatial light modulator. *Opt Express* (2013) 21:16541. doi:10.1364/OE.21.016541

8. Huo P-C, Zhang C, Zhu W-Q, Liu M-Z, Zhang S, Zhang S, et al. Photonic spin-multiplexing metasurface for switchable spiral phase contrast imaging. *Nano Lett* (2020) 4:2791–8. doi:10.1021/acs.nanolett.0c00471

9. Fang X-Y, Ren H-R, Gu M. Orbital angular momentum holography for high-security encryption. *Nat Photon* (2020) 14:102–8. doi:10.1038/s41566-019-0560-x

10. Ren H-R, Fang X-Y, Jang J, Burger J, Rho J, Maier SA, et al. Complex-amplitude metasurface-based orbital angular momentum holography in momentum space. *Nat Nanotechnol* (2020) 15:948–55. doi:10.1038/s41565-020-0768-4

11. Lavery MPJ, Speirits FC, Barnett SM, Padgett MJ. Detection of a spinning object using light's orbital angular momentum. *Science* (2013) 341:537–40. doi:10.1126/science.1239936

12. Berkhout GCG, Beijersbergen MW. Method for probing the orbital angular momentum of optical vortices in electromagnetic waves from astronomical objects. *Phys Rev Lett* (2008) 101:100801. doi:10.1103/PhysRevLett.101.100801

13. Padgett M, Bowman R. Tweezers with a twist. *Nat Photon* (2011) 5:343–8. doi:10.1038/nphoton.2011.81

14. Dholakia K, Cizmar T. Shaping the future of manipulation. *Nat Photon* (2011) 5:335–42. doi:10.1038/nphoton.2011.80

15. Huang S-Y, Zhang G-L, Wang Q, Wang M, Tu C-H, Li Y-N, et al. Spin-to-orbital angular momentum conversion via light intensity gradient. *Optica* (2021) 8:1231. doi:10.1364/OPTICA.435475

16. Bondarescu M, Thorne KS. New family of light beams and mirror shapes for future ligo interferometers. *Phys Rev D* (2006) 74:082003. doi:10.1103/PhysRevD.74.082003

17. Wang J. Twisted optical communications using orbital angular momentum. *Sci China Phys Mech Astron* (2019) 62:34201. doi:10.1007/s11433-018-9260-8

18. Bozinovic N, Yue Y, Ren Y-X, Tur M, Kristensen P, Huang H, et al. Terabitscale orbital angular momentum mode division multiplexing in fibers. *Science* (2013) 340:1545–8. doi:10.1126/science.1237861

19. He C, Shen Y, Forbes A. Towards higher-dimensional structured light. *Light Sci Appl* (2022) 11:205. doi:10.1038/s41377-022-00897-3

20. Wang A-D, Zhu L, Chen S, Du C, Mo Q, Wang J, et al. Characterization of ldpc-coded orbital angular momentum modes transmission and multiplexing over a 50-km fiber. *Opt Express* (2016) 24:11716. doi:10.1364/OE.24.011716

21. Krenn M, Fink M, Fickler R, Zeilinger A. Twisted photon entanglement through turbulent air across vienna. *Proc Natl Acad Sci U S A* (2015) 112: 14197–201. doi:10.1073/pnas.1517574112

22. Yan Y, Xie G-D, Lavery MPJ, Huang H, Ahmed N, Bao C-J, et al. High-capacity millimetre-wave communications with orbital angular momentum multiplexing. *Nat Commun* (2014) 5:4876. doi:10.1038/ncomms5876

23. Xie G-D, Ren Y-X, Yan Y, Huang H, Ahmed N, Li L, et al. Experimental demonstration of a 200-gbit/s free-space optical link by multiplexing laguerre-Gaussian beams with different radial indices. *Opt Lett* (2016) 41:3447. doi:10.1364/OL.41.003447

24. Fabre C, Treps N. Modes and states in quantum optics. *Rev Mod Phys* (2020) 92:035005. doi:10.1103/RevModPhys.92.035005

25. Shen Y, Rosales-Guzman C. Nonseparable states of light: From quantum to classical. *Laser Photon Rev* (2022) 16:2100533. doi:10.1002/lpor.202100533

26. Erhard M, Fickler R, Krenn M, Zeilinger A. Twisted photons: New quantum perspectives in high dimensions. *Light Sci Appl* (2017) 7:17146. doi:10.1038/lsa.2017.146

27. Erhard M, Krenn M, Zeilinger A. Advances in high dimensional quantum entanglement. *Nat Rev Phys* (2020) 2:365–81. doi:10.1038/s42254-020-0193-5

28. Mair A, Vaziri A, Weihs G, Zeilinger A. Entanglement of the orbital angular momentum states of photons. *Nature* (2001) 412:313–6. doi:10.1038/35085529

29. Fickler R, Campbell G, Buchler B, Lam PK, Zeilinger A. Quantum entanglement of angular momentum states with quantum numbers up to 10, 010. *Proc Natl Acad Sci U S A* (2016) 113:13642–7. doi:10.1073/pnas.1616889113

30. M-Terriza G, Torres JP, Torner L. Twisted photons. *Nat Phys* (2007) 3: 305–10. doi:10.1038/nphys607

31. Kong L-J, Liu R, Qi W-R, Wang Z-X, Huang S-Y, Wang Q, et al. Manipulation of eight-dimensional bell-like states. *Sci Adv* (2019) 5:eaat9206. doi:10.1126/sciadv.aat9206

32. Zhao S-M, Gong L-Y, Li Y-Q, Yang H, Sheng Y-B, Cheng W-W, et al. A large-alphabet quantum key distribution protocol using orbital angular momentum entanglement. *Chin Phys Lett* (2013) 30:060305. doi:10.1088/0256-307X/30/6/060305

33. Hu X-M, Xing W-B, Liu B-H, He D-Y, Cao H, Guo Y, et al. Efficient distribution of high-dimensional entanglement through 11 km fiber. *Optica* (2020) 7:738. doi:10.1364/OPTICA.388773

34. Romero J, Giovannini D, Franke-Arnold S, Barnett SM, Padgett MJ. Increasing the dimension in high-dimensional two-photon orbital angular momentum entanglement. *Phys Rev A* (2012) 86:012334. doi:10.1103/PhysRevA.86.012334

35. Di Lorenzo Pires H, Florijn HCB, Van Exter MP. Measurement of the spiral spectrum of entangled two-photon states. *Phys Rev Lett* (2010) 104:020505. doi:10.1103/PhysRevLett.104.020505

36. Anwar A, Prabhakar S, Singh RP. Size-invariant twisted optical modes for the efficient generation of higher-dimensional quantum states. *J Opt Soc Am B* (2021) 2976. doi:10.1364/JOSAB.436088

37. Canas G, Gomez ES, Baradit E, Lima G, Walborn SP. Engineering entangled photons for transmission in ring-core optical fibers. *Front Phys* (2021) 9:752081. doi:10.3389/fphy.2021.752081

38. Liu S-L, Zhou Z-Y, Liu S-K, Li Y-H, Li Y, Yang C, et al. Coherent manipulation of a three-dimensional maximally entangled state. *Phys Rev A* (2018) 98:062316. doi:10.1103/PhysRevA.98.062316

39. Kovlakov EV, Straupe SS, Kulik SP. Quantum state engineering with twisted photons via adaptive shaping of the pump beam. *Phys Rev A* (2018) 98:060301. doi:10.1103/PhysRevA.98.060301

40. Anwar A, Lal N, Prabhakar S, Singh RP. Selective tuning of hilbert spaces in states encoded with spatial modes of light. *New J Phys* (2020) 22:113020. doi:10.1088/1367-2630/abc783

41. Kyselaa J, Erharda M, Hochrainer A, Krenn M, Zeilinger A. Path identity as a source of high-dimensional entanglement. *Proc Natl Acad Sci U S A* (2020) 117: 26118–22. doi:10.1073/pnas.2011405117

42. Okoth C, Cavanna A, Santiago-Cruz T, Chekhova MV. Microscale generation of entangled photons without momentum conservation. *Phys Rev Lett* (2019) 123: 263602. doi:10.1103/PhysRevLett.123.263602

43. Torres JP, Alexandrescu A, Torner L. Quantum spiral bandwidth of entangled two-photon states. *Phys Rev A* (2003) 68:050301. doi:10.1103/PhysRevA.68.050301

44. Hua Y-L, Zhou Z-Q, Liu X, Yang T-S, Li Z-F, Li P-Y, et al. Annual-ring-type quasi-phase-matching crystal for generation of narrowband high-dimensional entanglement. *Phys Rev A* (2018) 97:013836. doi:10.1103/PhysRevA.97.013836

45. Abdelwahab I, Tilmann B, Wu Y, Giovanni D, Verzhbitskiy I, Zhu M, et al. Giant second-harmonic generation in ferroelectric $NbOI_2$. *Nat Photon* (2022).

46. Kang L, Bao H-G, Werner DH. Efficient second-harmonic generation in high Q-factor asymmetric lithium niobate metasurfaces. *Opt Lett* (2021) 46:633. doi:10.1364/OL.413764

47. Yang Q-Y, Liu Y, Gan X-T, Fang C-Z, Han G-Q, Hao Y, et al. Nonlinear bound states in the continuum of etchless lithium niobate metasurfaces. *IEEE Photon J* (2019) 1–9. doi:10.1109/JPHOT.2020.3024789

48. Parry M, Mazzanti A, Poddubny AN, Valle GD, Neshev DN, Sukhorukov AA, et al. Enhanced generation of nondegenerate photon pairs in nonlinear metasurfaces. *Adv Photon* (2021) 3:55001. doi:10.1117/1.AP.3.5.055001